PROCEEDINGS, 42nd Workshop on Geothermal Reservoir Engineering
Stanford University, Stanford, California, February 13-15, 2017
SGP-TR-212

Inferring geothermal reservoir processes at the Raft River Geothermal Field, Idaho, USA through modeling InSAR-measured surface deformation

Fang Liu[1, 2], Pengcheng Fu[3], Robert J. Mellors[3],
Mitchell Plummer[4], Tabrez Ali[5], Elena C. Reinisch[5], Qi Liu[2], Kurt L. Feigl[5]

[1] State Key Laboratory of Disaster Reduction in Civil Engineering, Tongji University, Shanghai, China

[2] Department of Geotechnical Engineering, Tongji University, Shanghai, China

[3] Lawrence Livermore National Laboratory, Livermore, CA, USA

[4] Idaho National Lab, ID, USA

[5] Department of Geoscience, University of Wisconsin, Madison, WI, USA

E-mail: fu4@llnl.gov

Keywords: THM coupled reservoir simulation; InSAR data; subsurface characterization; Raft River

ABSTRACT

Ground surface deformations detected with Interferometric Synthetic Aperture Radar (InSAR) provide valuable information for inferring subsurface reservoir processes that are difficult to observe directly. This study aims at building a reservoir model that honors the available geological, hydrological and geo-mechanical data and also produces ground surface deformation consistent with InSAR measurements. In our coupled thermo-hydro-mechanical (THM) model, the reservoir deforms as a result of the rock's poroelastic response to changes in hydrologic pressure and thermal expansion/contraction. The computations are performed using a massively parallel multi-physics code (GEOS) at the scale of the geothermal field. At Raft River, the results indicate that the observed deformation cannot be caused solely by pressure changes in the deep production reservoir, and that pressure increase in a shallower reservoir that accommodates the injected fluid (likely in the Salt Lake Formation) must be involved. The rising pressure in the shallow reservoir generates strong uplift at ground surface. The combination of this uplift with surface subsidence around the production wells creates a complex pattern of surface deformation in which the center of subtle subsidence significantly deviates from the location of the production wells. The net pressure in the shallow reservoir may gradually diffuse into the moderately permeable layer underneath, resulting in additional slow deformation. Therefore, the surface deformation captured by InSAR represents a combination of multiple mechanisms acting over different time scales. A parametric study suggests that the Bridge Fault Zone is likely a barrier, impeding laterally flow cross the fault, although the fault could serve as a fast flow path along the strike direction. The surface deformation data appear to be insensitive to the presence of the Narrows Structure (i.e., a poorly defined northeast-southwest trending structure within the deep geothermal reservoir), since removing the Narrows Structure from the model does not substantially change the modeled deformation pattern at the surface. A flow barrier likely exists to the east of the site, where the surface uplift forms a band striking from north to south. This case study demonstrates the utility of a forward model that honors available known information and THM coupled processes in understanding geothermal reservoir characteristics.

1. INTRODUCTION

The production of hot water from and the injection of cold water into a geothermal reservoir involve many thermal, hydrological, mechanical, and chemical processes. Monitoring and understanding these subsurface processes and their relationships could substantially benefit the development and operation of geothermal reservoirs. However, these processes are challenging and costly to quantify because of the great depths of geothermal reservoirs, the limited access to the depths (through wells), and the hostile environment to sensors (high pressure and high temperature). The measurement of ground surface deformation above the reservoir, particularly using Interferometric Synthetic Aperture Radar (InSAR), provides a promising means to infer subsurface processes through their ground manifestations (e.g. surface subsidence or uplift, as well as lateral movements). InSAR quantifies the ground deformation that occurs between the acquisition times of two radar images by computing the difference in the round-trip travel times of microwaves propagating from the sensor aboard a satellite to the ground (e.g., Massonnet and Feigl, 1998). Because of the broad spatial coverage, fine sensitivity (millimeter-level), and relatively low cost, this technique has received increasing utilization in geothermal fields (Ali et al., 2016a, b; Sarychikina et al., 2011; Oppliger et al., 2005; Vasco et al., 2002; Fialko and Simons, 2000; Massonnet et al., 1997). Comprehensive reviews of InSAR applications and advancements can be found in the literature (Burgmann et al., 2000; Prati et al., 2010; Hooper et al., 2012; Caduff et al. 2015). Currently, the advent of a new generation of commercial SAR satellites with tightly constrained orbits, rapidly repeating acquisitions, improved processing algorithms, and low-cost or free data (e.g., the Sentinel-1 mission operated by the European Space Agency), will greatly improve the availability and potential use of SAR data for monitoring geothermal fields.

The inference of subsurface features via InSAR data analysis is typically accomplished through inverse analyses based on analytical continuum mechanics models or fully numerical models. Commonly used analytical models include inflation of a spherical source (Mogi, 1958), a planar dislocation source (Okada, 1985), and a penny-shaped crack (Fialko and Simons, 2000) in elastic half-space. Analytic models are useful for inversion codes, which seek to minimize the difference between observations and synthetics and usually assume some sort of regularization. While these efforts generally match the observed signal, these methods provide little understanding of the fundamental physical processes other than approximate constraints on depth and lateral extent. Nor can they incorporate the complex geological, hydrological, and geo-mechanical data available. Therefore, inversion based on analytical methods do not reveal complex reservoir structure or processes (Oppliger et al., 2005). Numerical methods are capable of matching subsurface conditions in more detail (e.g. Ali et al., 2016a), but little work has been conducted using multi-physics models that match a full suite of subsurface processes such as fluid flow, heat transfer, and effective stress changes.

This study aims at developing a forward model for the Raft River geothermal field to reveal subsurface geothermal processes that yield surface deformation consistent with InSAR observations. We recognize two challenges for such modeling. First, a complete description of a subsurface reservoir is generally unavailable. Even though many geophysical techniques such as 3D magnetotelluric surveying (Maris et al., 2012; Newman et al., 2008), 3D vertical seismic profiling (Newman and Petrov, 2016; Queen et al., 2016), and surface seismic reflection (Casteel et al., 2016; Queen et al., 2016) have been developed and advanced in recent years, data for a given field, such as the Raft River field, are still limited compared with the required information for constraining a high fidelity subsurface model. Second, geothermal reservoir deformation could result from tightly-coupled subsurface processes that include thermal contraction/expansion (thermo-mechanical), rock dilation/compression due to hydraulic pressure change (hydro-mechanical), chemical precipitation/dissolution (chemical-mechanical), or even fault motion. Proper differentiation of these mechanisms is necessary to build a model that yields the observed deformation for the correct reasons. To overcome these challenges, we adopt a data-driven and process-oriented approach by: (1) collecting and integrating a wide variety of available data for the field, (2) identifying the main mechanisms governing the observed deformation, (3) employing a physics-based thermo-hydro-mechanical (THM) fully coupled numerical model, (4) determining otherwise unconstrained model parameters based on an investigation of the effects of these parameters and the associated processes, and (5) finally reducing the uncertainties in the resultant model by performing a sensitivity analysis. These aspects of the work are described in the subsequent sections.

2. BACKGROUND OF THE RAFT RIVER GEOTHERMAL FIELD

The Raft River geothermal site is located in the Raft River Valley in southeastern Idaho, 100 miles northwest of Salt Lake City, UT. It was designated a Known Geothermal Resource Area in 1971 and operated as a geothermal demonstration plant from late 1981 to June 1982 (Covington, 1980). Afterwards, no production was carried out at the site until US Geothermal Inc. acquired it in 2002. After upgrading existing wells and drilling new wells, a binary 13 MW plant has been in operation since January 2008, extracting roughly 300 kg/s total fluid at bottom-hole temperatures ranging from 133 ^{o}C to 149 ^{o}C (Ayling et al., 2011).

The primary geothermal reservoir at the site resides in the approximately 150 m thick layer of Elba Quartzite in the Precambrian basement underlying the Raft River basin (Dolenc et al., 1981). The top 300 m of the basin defines the Raft River Formation, composed of inter-fingering, lenticular, fluvial, alluvial and loess sediments. Below the Raft River Formation underlies the Salt Lake Formation with an average thickness of about 1200 m, consisting of Miocene-Pliocene lacustrine deposits, and volcanic tuffs and flows. Siltstone and sandstone of the Salt Lake Formation have been deformed by numerous high angle micro-faults and bedding convolutions. The basement contact of the Salt Lake Formation gently dips to the east and has been inferred to be a detachment surface (Williams et al., 1982). Geo-mechanical data at the site are sparse. Mechanical tests on samples extracted from the base of the Tertiary deposits in the Salt Lake Formation suggest that the Young's modulus of the samples ranges from 12 to 19 GPa and the Poisson's ratio is approximately 0.15 (Jones et al., 2011).

The geothermal reservoir is considered to be fault-controlled, as shown in Figure 1. The Bridge Fault Zone is a north-south striking normal fault west of the production wells. This fault steeply dips from the ground surface and flattens at the basement-sediment contact. Gravity and magnetic survey data suggest that the Bridge Fault terminates against another major structure, the Narrows Zone (also termed as the Narrows Structure), a poorly defined northeast-southwest trending structure within the Precambrian rocks (Bradford et al., 2013). The deep upflow zone of the geothermal system is speculated to be controlled by the intersection of the Bridge Fault with the Narrows Structure (Williams et al., 1976; Mabey et al., 1978; Dolenc et al., 1981). The Narrows Structure has been interpreted to be a basement shear (Mabey et al. 1979), and it appears as an important structural discontinuity that divides the geothermal system into two major compartments (Bradford et al., 2013) as corroborated by geochemical investigations (Ayling and Moore, 2013; Ayling et al., 2011). Wells drilled northwest of the Narrows Structure produce lower salinity waters from the Precambrian rocks than do wells to the southeast. This indicates that the Narrows Structure represents a flow barrier (Ayling and Moore, 2013; Ayling et al., 2011).

In the original plan, production was from the deep aquifer at the depth of approximately 1100-1500 m (Dolenc et al., 1981) via four production wells (i.e., RRG-1, -2, -3, -5), whereas injection was into the intermediate aquifer at the depth of approximately 500-700 m (Dolenc et al., 1981) with three injection wells (i.e., RRG-4, -6, -7) to avoid temperature drawdown of the deeper hydrothermal resource (Covington, 1980; Dolenc et al., 1981; Millar, 1979). Since U.S. Geothermal acquired the lease, the deep wells were deepened or sidetracked and two additional wells were drilled. As shown in Figure 1, the site currently operates four production wells (RRG-1, -2, -4, -7), all of which penetrate the Cenozoic sediments and reach Precambrian basement at approximately 1400 m depth on the northwest side of the field, and approximately 1750 m depth on the southeast side of the field (Ayling and Moore, 2013). Wells RRG-3, -6 and -11 inject recycled brine at about 62.2^{o}C (Millar, 1979). The injection wells have long open-hole sections in the Tertiary sedimentary deposits within the Salt Lake Formation, whereas the production wells are cased in this depth interval. Logging in RRG-6 (uncased from the depth of 515 m to its total depth of 1185 m) indicates that a significant fraction of the injected fluids leaves the borehole

immediately below the casing (Ahmed et al., 1979; Spencer, 1979). This implies the presence of a major thief zone, which is seen in nearly all the deep wells (Ahmed et al., 1979; Spencer, 1979).

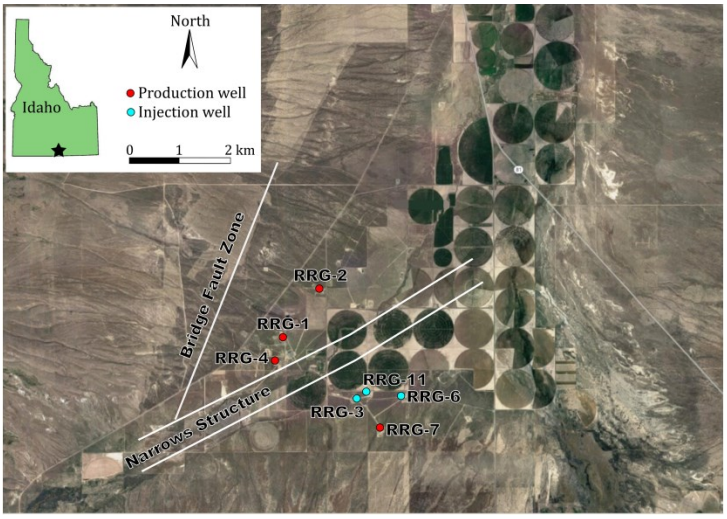

Figure 1: Location, well layout, and important known geologic features of the Raft River geothermal site. Current production wells are denoted by red dots and injection wells by blue dots.

3. INSAR DATA AND KEY SURFACE DEFORMATION FEATURES

Following earlier studies by Aly and Brawner (2014) and Ali et al. (2016), we analyze data from six interferometric pairs developed from the SAR images (Envisat, C-band, ascending) spanning the time interval between 2007 and 2010 at the Raft River site collected by the Envisat mission (McLeod et al., 2008). This is a subset of data analyzed by Ali et al. (2016b). All the interferometric pairs use the image acquired on March 11, 2007 as the reference (or "master") image. This image is the last one available before geothermal production began. A pair of SAR images forms an interferogram that maps the change in phase during the time interval between the two acquisition dates. Originally expressed in terms of phase change, the interferogram is converted into a map of the change in range, i.e., the vector displacement field projected along the "line of sight" between the radar sensor aboard the satellite and the pixel on the ground by a procedure known as "unwrapping". The topographic contribution in the interferograms is removed using a digital elevation model with 1 arc-second posting from the Shuttle Radar Topographic Mission (Farr et al., 2007). Unwrapping is performed using the "statistical-cost, network-flow phase-unwrapping algorithm" developed by Chen and Zebker (2001). As the incidence angle for Envisat is approximately 23° from vertical, the range change is predominantly sensitive to the vertical component of the displacement field. Since it is not possible to uniquely distinguish between the vertical and horizontal components of displacement vector field using this dataset, a fair comparison would require projecting the simulated ground deformation vector onto the line-of-sight direction. However, we directly compare the overall pattern of the unwrapped range change towards the satellite with the simulated vertical surface deformation pattern in this preliminary study. This discrepancy should not affect the interpretation of the subsurface processes underlying the observed ground deformation pattern, and will be resolved in the next phase of this work.

The upper row of Figure 4 shows a strong uplift signal over an area approximately centered at the injection wells, whereas subtle subsidence is observed to the west of the production wells. The transition zone separating the uplifting and subsiding areas appears to be associated with the Bridge Fault. These signatures consistently appear in all the interferometric pairs from Envisat. Both the uplift and subsidence are transient, as found previously by Ali et al. (2016), using the same SAR data. The magnitudes of uplift and subsidence each increased in absolute value during the first two years of the geothermal production. Subsequently, the surface deformation remained largely unchanged during the next six years (Ali et al. 2016).

4. A THM COUPLED MODEL

4.1 Modeling methodology

As discussed above, mechanical deformation of reservoir rocks and overlaying rocks can be caused by thermo-mechanical (TM), hydro-mechanical (HM), and chemico-mechanical (CM) processes. In this study, we only consider coupled thermo-hydro-mechanical (THM) processes and ignore any potential chemical aspects for the following reasons. First, the surface deformation observed in the InSAR data window is most likely dominated by hydro-mechanical coupling because the uplift near the injection wells leveled off two years after the commencement of the production. As fluid circulation has continued since early 2008, the manifestations of TM and CM processes would have had also continued in a more or less monotonic fashion. The hydrological processes, on the other hand, are expected to reach a steady or pseudo-steady state in a relatively short period. Second, there are not plausible chemical reactions that can achieve the observed magnitude of surface deformation. The volume increase within a radius of 3 km around the injection wells in the first two years of production is approximately (mean upheave times the area) to be one million m^3 and the total circulation volume in the same time window is approximately 20 million m^3. Assuming the mean density of the precipitated mineral to be 2.7 g/cm^3, 135 grams of minerals would have to be precipitated per liter of injected fluid. The chemical compositions of the produced fluid at Raft River published by Ayling and Moore (2013) do not support such a hypothesis.

We construct a numerical model using GEOS, a high performance computing (HPC) platform developed at the Lawrence Livermore National Laboratory (LLNL) (Settgast et al., 2016), to simulate the coupled THM processes at the Raft River site. We idealize the rock matrix as a poroelastic medium subjected to single-phase fluid (i.e. water) flow. The reservoir deforms as a result of poroelastic effects driven by pore pressure change and thermal expansion/contraction. The essential processes/mechanisms involved include: (1) Fluid flow in multiple rock formations with distinct permeabilities; (2) convective heat transfer associated with the fluid flow through rock matrix, conductive heat transfer in the rock matrix, and heat exchange between the flowing fluid and the surrounding rock body; (3) the change of effective stress caused by the non-uniform cooling of the rock body and change of pore water pressure; and (4) the deformation of the rock matrix as the effective stress changes. The first two processes are simulated by a combined flow and heat transfer solver while the other two processes are simulated through a solid mechanics solver. We use an implicit time integration scheme in the flow solver, and the time step size is adaptively adjusted. Generally, small time steps are required in the beginning of the heat production due to the high degree of transience of the system. As the system evolves into a semi-steady state, relatively long time steps suffice. In each time step, the two solvers alternate. The fields of temperature and fluid pressure from the flow and heat solver are used in the solid solver for computing the deformation of the rock matrix.

The flow and heat transfer solver combines fluid flow and heat transfer in rock matrix. We use a finite volume formulation to solve the independent state variables, namely fluid pressure P and temperature T, for 3D 8-node hexahedral elements. The coupled single-phase flow and heat transfer in porous medium are governed by the principle of mass and energy conservation. The mass conservation equation for compressible fluid is:

$$\frac{\partial(\rho\varphi)}{\partial t}+\nabla\cdot(\rho\mathbf{v})=\Gamma \tag{1}$$

where ρ is the fluid density; ϕ is the rock porosity; t is time; $\mathbf{v}$ is the fluid velocity vector; and Γ is a source/sink term. According to Darcy's law, fluid velocity vector $\mathbf{v}$ is calculated as:

$$\mathbf{v}=-\frac{\mathbf{k}}{\mu}(\nabla P-\rho\mathbf{g}) \tag{2}$$

where $\mathbf{k}$ is the intrinsic permeability tensor of the rock matrix; μ is the fluid dynamic viscosity; and g is the gravity acceleration vector. The current study assumes the permeability of rock matrix to be isotropic, so the permeability tensor reduces to the permeability scalar k. Substituting Equation (2) into Equation (1) yields

$$\frac{\partial(\rho\varphi)}{\partial t}-\nabla\cdot\left[\rho\frac{k}{\mu}(\nabla P-\rho\mathbf{g})\right]=\Gamma \tag{3}$$

Fluid density ρ depends on fluid pressure and temperature, as approximated by the following analytical function

$$\rho=\rho_r e^{\left[\beta_f(P-P_r)+\alpha_f(T-T_r)\right]} \tag{4}$$

where ρ_r, P_r, T_r, β_f, and α_f are the fluid density, pressure, temperature, fluid compressibility, and fluid thermal expansion coefficient, respectively, in a known reference state.

The governing equation describing the energy balance over the fluid phase and the solid phase in a porous medium is

$$\frac{\partial}{\partial t}\left(\phi\rho C_f T+(1-\phi)\rho_s C_s T\right)+\nabla\cdot\left(\rho C_f T\mathbf{v}\right)=\nabla\cdot(K_m\nabla T)+Q \tag{6}$$

where C_f is the specific heat capacity of the fluid; ρ_s is the rock solid density; C_s is the specific heat capacity of the rock solid; K_m is the thermal conductivity of the rock matrix; and Q is a source/sink term of heat.

Once the flow solver obtains the pore pressure and temperature fields, they are used in the poroelastic solid mechanics solver as known boundary conditions to solve for the displacement field. Because the pore compressibility used in the flow solver for each formation is consistent with bulk modulus and porosity of the same formation in the solid solver, the effects of the porosity change resulting from the solid deformation on the flow field are handled consistently between the two solvers, eliminating the need for iterative coupling between the solvers within each time step.

4.2 Model set-up

Figure 2 illustrates the conceptual model of the Raft River geothermal system used in the current study, composed of six horizontal strata of various thicknesses determined based on data in the literature. The elevation at the ground surface is about 1500 m above the mean sea level. Depths referred to by the current work are all from the ground surface. We simplify the actual geological profile by leveling the strata, as the strata only gently deviate from the horizontal direction and detailed terrain have only secondary effects on the resultant ground deformation. Figure 3 shows the FEM mesh used in the simulation, in the WGS 84/UTM Zone 12T coordinate system. The mesh covers an area of 25 km by 25 km up to a depth of 2 km. It consists of 594,000 hexahedral elements with element dimensions

ranging from 100 m to 200 m. Despite the relative coarseness, the mesh resolution is sufficient to capture the primary length scale of concerned processes as the area affected by the deformation span several kilometers.

Table 1 lists the model parameters used in the baseline case. The permeability of the injection reservoir and the geothermal reservoir is based on available flow testing data documented in the literature (Ahmed et al., 1979; Glaspey et al., 2008). Other parameters are chosen from typical ranges of different types of deposits or rocks, with the Young's modulus values adjusted through preliminary runs to match the magnitude of the simulated ground surface deformation. In the baseline case, we model the Bridge Fault and the Narrows Structure as impervious barriers of flow, and therefore an extremely low permeability is assigned to cells representing these features. The initial temperature field in the ground is set in such way that the temperature in geothermal and injection reservoirs is 145 ºC and 100 ºC, respectively, and linearly varies with depth elsewhere. Initial hydrostatic condition is assumed, consistent with available well logs (Glaspey et al., 2008). The production wells and injection wells are present in the numerical model as boundary conditions; the four production wells each serves as a sink with a flow rate of 0.075 m^3/s, and the three injection wells each serves as a source with flow rate of 0.1 m^3/s at temperature 65 ºC. Along the four lateral sides of the model, pressure and temperature boundary conditions consistent with the initial conditions at the corresponding depths are enforced. The bottom of the model is assumed to be impermeable.

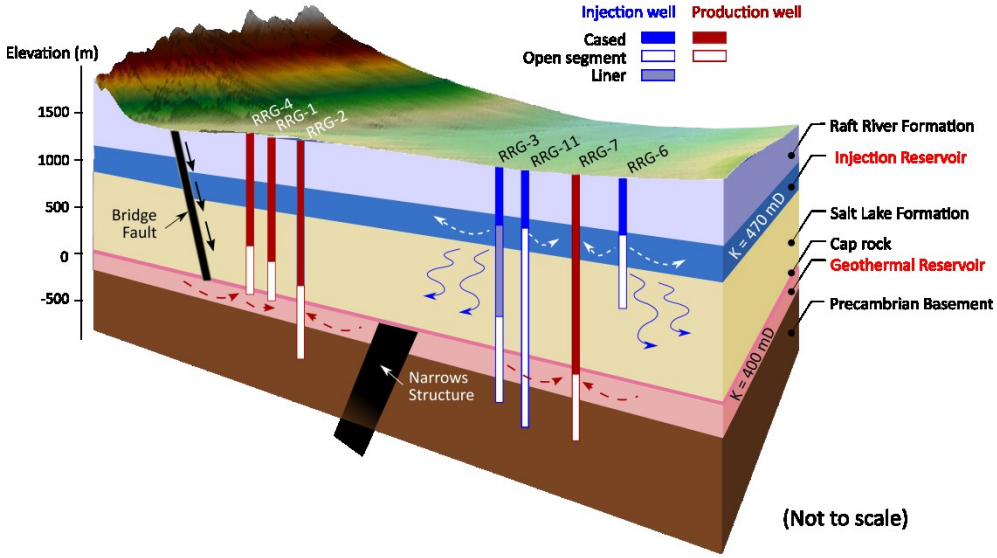

Figure 2. Schematic illustration of a conceptual model of the Raft River geothermal system. The elevation axis only provides a rough reference scale and the figure is not to scale in the horizontal direction.

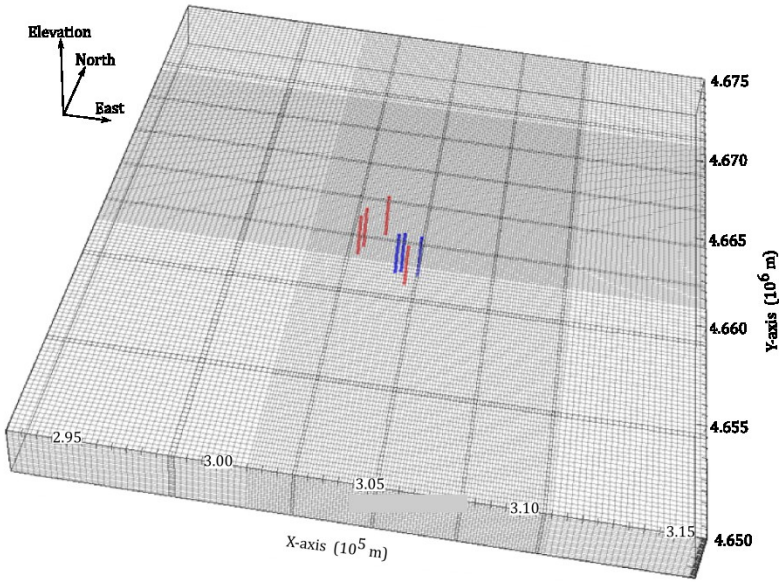

Figure 3. The finite element mesh of the site. The red and blue lines illustrate the production and injection wells, respectively. The model uses the WGS 84/UTM Zone 12T coordinate system.

Table 1. Model parameters used in the baseline case

Layer	Thickness (m)	Permeability (mD)	Porosity	Young's modulus (GPa)	Poisson's ratio	Pore compress. (10^{-9} Pa^{-1})
Raft River Formation	500	10^{-2}	0.05	10	0.2	3.42
Injection reservoir	300	470	0.15	3	0.2	3.40
Salt Lake Formation	600	1	0.1	8	0.2	2.03
Cap rock	100	10^{-6}	0.05	30	0.2	1.14
Geothermal reservoir	100	400	0.15	5	0.2	2.04
Precambrian basement	400	10^{-6}	0.05	30	0.2	1.14

5. RESULTS

5.1 The baseline simulation

The lower row of Figure 4 presents the spatial distribution of the vertical ground deformation generated from the numerical model on four dates in comparison with the corresponding InSAR data in the lower row. Note that the InSAR data use the satellite image on March 11, 2007 as the baseline whereas we assume fluid circulation started on January 1, 2008 and continued without interruption. A negative displacement means subsidence (i.e. cold color in the scale bar) and a positive value means uplift (i.e. hot color). The simulation results agree with the InSAR observations in terms of the magnitude and general spatial pattern of the ground deformations. As suggested by the numerical results, the ground deformations become noticeable in the order of centimeters after two months of production, forming two circular features, i.e. a subsiding bowl and a heaving dome. The dome is approximately centered at the three injection wells (marked as blue squares), whereas the subsiding area is in the northwest of the production wells (marked as pink squares). As the production continues, the two circular features expand spatially with intensified color, since the subsurface goethermal operation causes greater deformation in a wider area as time goes. As shown in Figs. 4c and 4d, the area of subsidence nearly saturates in size after approximately two years of plant operation, and similar patterns are also noted in InSAR observation (Figs. 4g and 4h). The uplift spreads more widely along the east-west direction in the simulation than that in the observation. This discrepancy suggests that there could be flow barriers to the east and west of the wells that constraining the flow field. This hypothesis can be tested using the same model.

Figure 5 shows the simulated vertical ground deformation over time at two locations (i.e. points A and B marked with stars in Fig. 4h). The InSAR data at the same locations are superimposed in the same figure for comparison. As a result of pore pressure increase due to injection, the simulated uplift at point A increases very rapidly during the first two years of production and reaches a peak of 125 mm after about 7.5 years of operation. Afterwards, the uplift declines slightly, since the pressure-induced volumetric expansion reaches a steady state while the thermal-contraction effect starts to dominate the deformation. In contrast, the ground at point B settles over time due to reduced pore pressure where the production wells locate. The subsidence started to decrease after one year of operation, because the ground heaving area expands laterally and intervenes the subsiding area. This intervention also shifts the uplifting area toward northwest of the production wells. The insert shows a good agreement between the InSAR measurement and the simulation in a short period in which InSAR data are available.

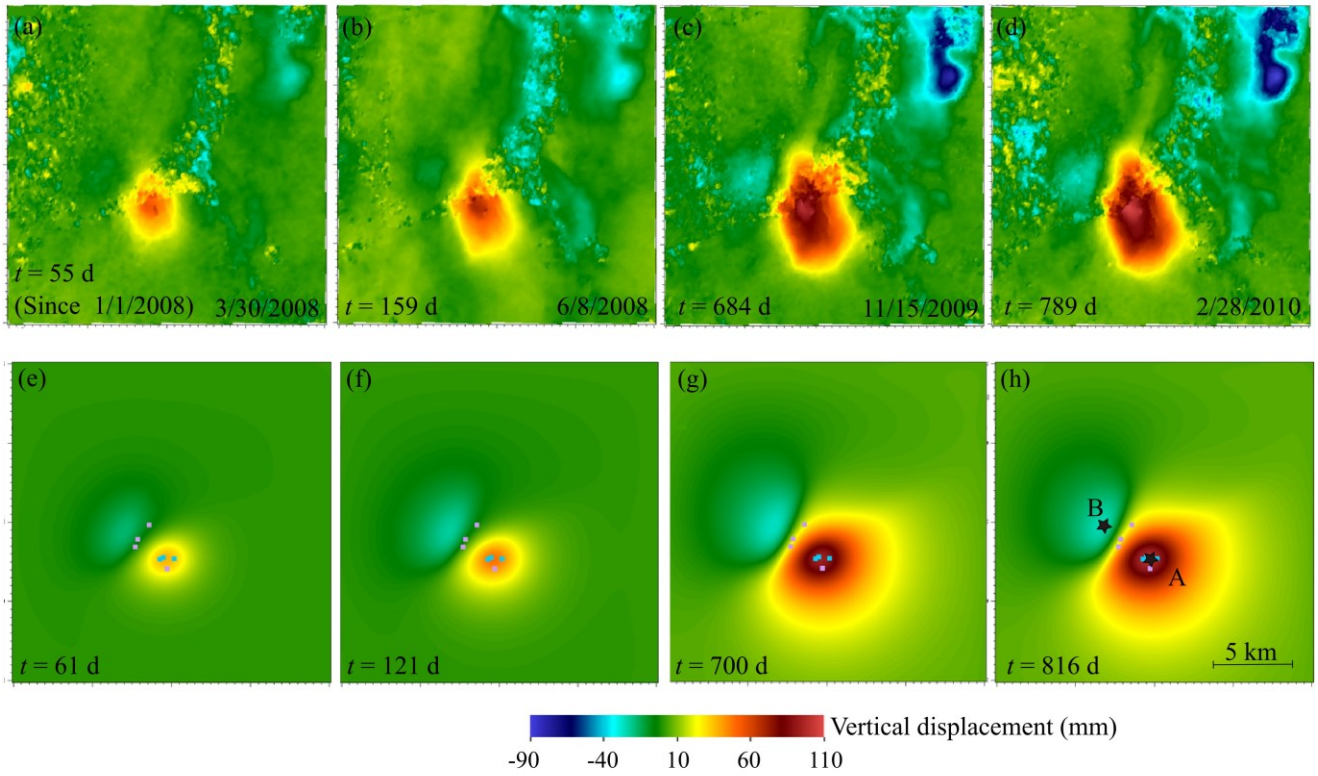

Figure 4. Maps of ground surface displacement showing the evolution of ground deformation over time. The upper row shows the InSAR observations. The lower row shows model prediction of vertical deformation. The longitude and latitude of the bottom left corner of the frame are (N42º1'13.2", W113º28'33.7"). The InSAR images use the SAR image on March 11, 2007 as the reference epoch, whereas fluid circulation and therefore ground deformation is assumed to start on January 1, 2008. Upward displacement is reckoned positive.

5.2 Contribution to the total deformations from individual layers

The injection reservoir (500-800 m from the ground surface) and the Salt Lake Formation (800-1400 m from the ground surface) are the two main layers that contribute to the ground heave. The pressure rapidly builds up in the shallow reservoir due to injection and causes rapid deformation in the ground. The net pressure gradually diffuses towards the Salt Lake Formation, resulting in subsequent deformation. The surface deformation is the combination of these two processes at different time scales. To investigate their respective contributions, we conducted additional simulations by setting Biot coefficients in layers other than the layer being considered to zero so that we can isolate the contribution of each layer to the total deformation. Figure 5 shows the ground uplift over time at point A (as shown in Fig 4h) contributed by the injection reservoir and by the Salt Lake Formation separately. The pore pressure in the injection reservoir increases in a rapid response to injection. However, the pore pressure increase at a lower rate in the Salt Lake Formation since this layer sees the front of pore pressure change later after the pore pressure diffuses from the injection reservoir. Interestingly, the deformation contributed by the injection reservoir saturates earlier (at about 1 year) than that by Salt Lake Formation (at about 4 years) because of various time scale of pressure change in different layers.

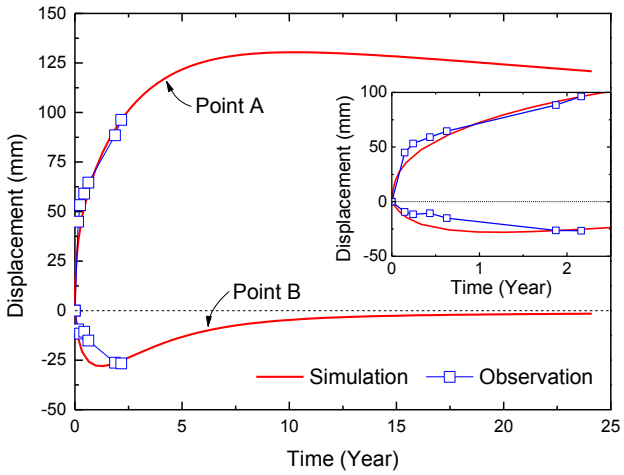

Figure 5. The vertical ground deformations over time at two locations (marked in Fig. 4h) according to the numerical simulation and InSAR measurement. The insert shows the same data in a shorter period.

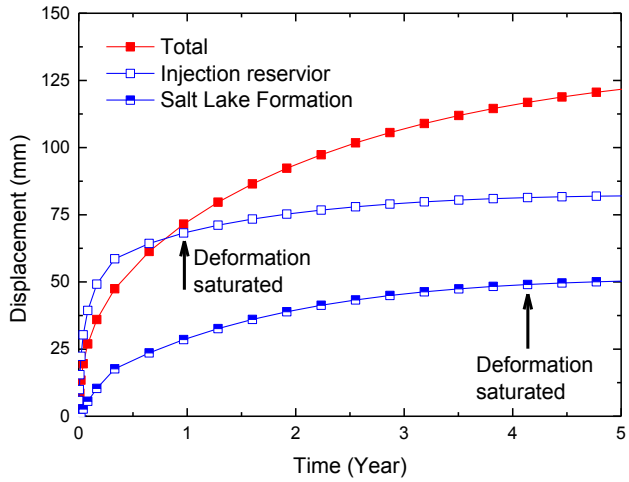

Figure 6. The contributions of individual layers to the uplift at point A (marked in Fig. 4h)

5.3 The role of the faults

Subsurface geological discontinuities are often poorly-defined with limited information about their effects on flows. Although we have assumed that the Bridge fault and the Narrows Structure both act as flow barriers in the baseline simulation, a faulted zone can actually function as either a barrier or a high-permeability channel for flow. It is noteworthy that the Narrows Structure was somewhat vaguely inferred from geochemistry studies (Ayling & Moore 2013; Ayling et al. 2011) and hydraulic fracturing responses (Keys, 1980). To further assess the presence and properties of the two geological structures (i.e. the Bridge Fault and the Narrows Structure), we conducted two additional simulations, one without Narrows Structure, and the other with permeable Bridge Fault but impervious Narrows Structure. Except for the parameters associated with the two structures, other parameters remain the same as in the baseline case.

Figure 7 compares the results obtained from the two additional simulations with that from the baseline case. Removal of the Narrows Structure (Fig. 7b) only slightly affects the transition pattern between uplift and subsidence at the surface. Without the Narrows Structure, the geothermal reservoir is no longer partitioned, and thus the pressure build-up due to injection diffuses more, resulting in a slight reduction of ground deformation. Nevertheless, the surface deformation is not very sensitive to the presence of the deeply-buried Narrows Structure. In contrast, making Bridge Fault a fast flow path greatly alters the ground deformation pattern and also decreases the magnitude, reducing the maximum uplift at the surface after 700-day production from approximately 100 mm to 60 mm. According to our interpretation of flow test results (i.e., RRG-4 flow and pressure buildup test reported by Glaspey et al. [2008]) and simulations of the flow tests (not presented in this paper), the Bridge fault could serve as a fast flow path along the fault direction. However, this fault is likely a barrier impeding flow cross the fault in order to result in the ground deformation that is consistent with InSAR observations spatially and temporally.

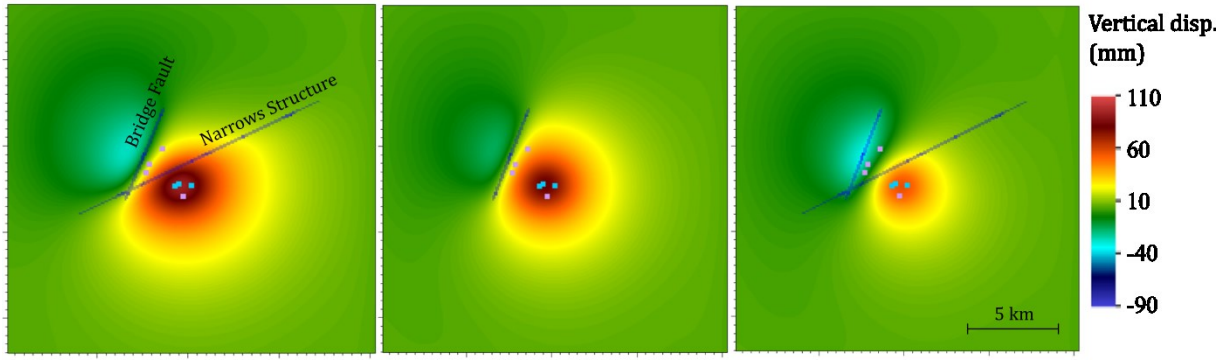

Figure 7. The effect of geological discontinuities on the patterns of vertical ground deformation after 700 days of production: (a) the baseline case; (b) the case without Narrows Structure; and (c) the case with permeable Bridge fault.

6. SUMMARY

This study presents a forward THM-coupled numerical modeling effort to understand the subsurface geothermal processes that produce ground deformation observed by InSAR at the Raft River geothermal site. The results support the hypothesis that the injection reservoir is much shallower than the geothermal reservoir. The rising pressure in the injection reservoir generates strong surface uplift while pressure drawdown in the deeper geothermal reservoir causes much subtler surface subsidence around the production wells. The combination of these two processes generated a complex pattern of surface deformation. A flow barrier likely exists to the east of the site, generating the observed surface uplift pattern that strikes linearly southwards rather than radially outward. A sensitivity study suggests that the Bridge Fault is likely a barrier impeding flow cross the fault, although the fault itself could serve as a fast flow path along the fault's strike direction. The modeled surface deformation pattern does not depend on whether or not the Narrows Structure is included in the simulation. Accordingly, we can neither support nor dismiss the hypothesized Narrows Structure.

The present study demonstrates the merit of a multi-physics forward model in understanding geothermal reservoir characteristics and subsurface processes. This forward-modeling approach honors the available known information and accounts for the coupling between thermal, hydrologic, and mechanical processes. The simulation reproduces the essential features of the ground deformation observed in the InSAR measurements.

For practical reservoir assessment and management considerations, the modeling results provide useful information about the flow system, including the vertical compartmentalization of the reservoir, the role of the Bridge Fault, the potential existence of previously unknown flow barriers, and the evolving extent of the pressure plume. Additional modeling and analysis could predict the surface deformation signatures of cooling fronts in the reservoir, which the team is pursuing in the next phase of the work. It should be emphasized that the effectiveness of the modeling strategy and the utilities of the modeling results highly depend on existing knowledge of the fundamental characteristics of the reservoir. A coherent conceptual model corroborated by multiple aspects of evidence is an important prerequisite for valid, useful modeling. In parallel to modeling the Raft River Geothermal Field, we also attempted to model the InSAR observations at the Brady's Hot Springs geothermal field in Nevada (Ali, et al., 2016) using a similar approach. There, the limited information available about the reservoir (e.g., Holt, et al., 2004) has heretofore impeded the development of coherent conceptual model. To address this issue, the PoroTomo project should provide additional constraints on the geo-mechanical structure of the reservoir (Feigl et al., 2016; Feigl and PoroTomo Team, 2017).

ACKNOWLEDGEMENTS

We thank Joseph Moore and Ian Warren for helpful discussions. The work at Lawrence Livermore National Laboratory was performed under the auspices of the U.S. Department of Energy under Contract DE-AC52-07NA27344 (LLNL-CONF-719223). The first author's visit LLNL to perform part of this collaborative research was supported by both LLNL and the Chinese National Natural Science Foundation (grant No. 41572267). The work at the University of Wisconsin-Madison was partly supported by grants DE-EE0005510 and DE-EE0006760 from the Geothermal Technologies Office of the U.S. Department of Energy. Raw SAR data from the Envisat satellite missions operated by the European Space Agency (ESA) are copyrighted by ESA and were provided through the WInSAR consortium at the UNAVCO facility. Elena C. Reinisch is supported by the National Science Foundation Graduate Research Fellowship under grant DGE-1256259.

REFERENCES

Ahmed, U., Wolgemuth, K.M., Abou-Sayed, A.S., Jones, A.H.: Injection Capability At the Raft River Geothermal Site, *Proceedings*, the 5th Workshop on Geothermal Reservoir Engineering, Stanford, CA (1979), pp. 29–39.

Ali, S.T., Akerley, J., Baluyut, E.C., Cardiff, M., Davatzes, N.C., Feigl, K.L., Foxall, W., Fratta, D., Mellors, R.J., Spielman, P., Wang, H.F., Zemach, E.: Time-series analysis of surface deformation at Brady Hot Springs geothermal field (Nevada) using interferometric synthetic aperture radar, *Geothermics* **61**, (2016a), 114–120.

Ali, S. T., Akerley, J., Baluyut, E. C., Davatzes, N. C., Lopeman, J., Moore, J., Plummer, M., Spielman, P., Warren, I., and Feigl, K. L.: Geodetic Measurements and Numerical Models of Deformation: Examples from Geothermal Fields in the Western United States, *Proceedings*, the 41st Workshop on Geothermal Reservoir Engineering, Stanford, CA (2016b), SGP-TR-209.

Aly, M. H., Brawner, E. V.: Contemporary InSAR measurements of ground deformation in the Snake River Plain and its adjacent basin-range province, Idaho, Proceedings, Geological Society of America, Rocky Mountain (66th Annual) and Cordilleran (110th Annual) Joint Meeting, (2014). https://gsa.confex.com/gsa/2014RM/webprogram/Paper238838.html

Ayling, B., Molling, P., Nye, R., Moore, J.: Fluid geochemistry at the Raft River geothermal field, Idaho, USA: New data and hydrogeological implications, *Proceedings*, the 36th Workshop on Geothermal Reservoir Engineering. Stanford, CA (2011), SGP–TR–191, DOI:10.1016/j.geothermics.2013.02.004

Ayling, B., Moore, J.: Fluid geochemistry at the Raft River geothermal field, Idaho, USA: New data and hydrogeological implications, *Geothermics* **47**, (2013), 116–126. DOI:10.1016/j.geothermics.2013.02.004

Bradford, J., Mclennan, J., Moore, J., Glasby, D., Waters, D., Kruwell, R., Bailey, A., Rickard, W., Bloomfield, K., King, D.: Recent developments at the Raft River geothermal field, *Proceedings,* the 38th Workshop on Geothermal Reservoir Engineering, Stanford, CA (2013), SGP–TR–198.

Burgmann, R., Rosen, P.A., Fielding, E.J.: Synthetic aperture radar interferometry to measure Earth's surface topography and its deformation. Annual Review of Earth and Planetary Sciences, **28**, (2000), 169-209

Caduff, R., Schlunegger, F., Kos, A., Wiesmann, A.: A review of terrestrial radar interferometry for measuring surface change in the geosciences. *Earth Surface Processes and Landforms*, **40**(2), (2015), 208-228.

Casteel, J., Mellors, R.J.: Estimating Subsurface Permeability with 3D Seismic Attributes : A Neural Net Approach, *Proceedings*, the 41st Workshop on Geothermal Reservoir Engineering, Stanford, CA (2016) pp. 1–8.

Chen, C.W. and Zebker, H.A., 2001. Two-dimensional phase unwrapping with use of statistical models for cost functions in nonlinear optimization. JOSA A, 18(2), pp.338-351.

Covington, H.R.: Subsurface geology of the Raft River geothermal area, Idaho. *Geotherm. Resour. Counc. Trans*. **4**, (1980), 113–115.

Dolenc, M.R., Hull, L.C., Steve A. Mizell, Russell, B.F., Skiba, P.A., Strawn, J.A., Tullis, J.A., Garber, R.: *Raft River geoscience case study*, EG&G, Idaho, Inc. (1981).

Farr, T.G., Rosen, P.A., Caro, E., Crippen, R., Duren, R., Hensley, S., Kobrick, M., Paller, M., Rodriguez, E., Roth, L. and Seal, D., 2007. The shuttle radar topography mission. Reviews of geophysics, 45(2).

Feigl, K. L., M. A. Cardiff, X. Zeng, N. E. Lord, C. Lancelle, L. Parker, E. C. Reinisch, David Lim, S. T. Ali, D. Fratta, C. H. Thurber, H. F. Wang, M. Robertson, J. Lopeman, C. Kreemer, C. Morency, N. C. Davatzes, PoroTomo Team, T. Coleman, and D. E. Miller (2016), Overview and Preliminary Results from the PoroTomo project at Brady Hot Springs, Nevada: Poroelastic Tomography by Adjoint Inverse Modeling of Data from Seismology, Geodesy, and Hydrology (abstract #H13O-02), in Fall Meeting Amer. Geophys. Un., San Francisco. https://agu.confex.com/agu/fm16/meetingapp.cgi/Paper/119495

Feigl, K. L., and PoroTomo Team (2017), Overview and Preliminary Results from the PoroTomo Project at Brady Hot Springs, Nevada: Poroelastic Tomography by Adjoint Inverse Modeling of Data from Seismology, Geodesy, and Hydrology, paper presented at Stanford Geothermal Workshop, Stanford University.

Fialko, Y., Simons, M.: Deformation and seismicity in the Coso geothermal area, Inyo County, California: Observations and modeling using satellite radar interferometry. *J. Geophys. Res*. **105** (2000), 21781–21793. DOI:10.1029/2000JB900169.

Glaspey, D., Kitz, K., Teplow, B., Sanyal, S., Faulder, D.: *Final Technical Report for Resource Confirmation Testing at the Raft River Geothermal Project* , Cassia County , Idaho (2008).

Holt, R., Cambell, D., Matlick, S.: Reservoir Simulation of Brady's Geothermal Field, Nevada. *Geotherm. Resour. Counc. Trans.* **28**, (2004), 589-593.

Hooper, A., Bekaert, D., Spaans, K., Arikan, M.: Recent advances in SAR interferometry time series analysis for measuring crustal deformation, *Tectonophysics*, **514**, (2012), 1-13.

Jones, C., Moore, J., Teplow, W., Craig, S.: Geology and Hydrothermal Alteration of the Raft River Geothermal System , Idaho, *Proceedings*, the 36h Workshop on Geothermal Reservoir Engineering, Stanford, CA, (2011), SGP–TR–191.

Keys, W. S.: The application of the accoustic televiewer to the characterization of hydraulic fractures in geothermal wells. Geothermal Reservoir Well Stimulation Symposium, San Francisco, USA (1980), 176-202.

Mabey, D.R., Hoover, D.B., O'Donnell, J.E., Wilson, C.W.: Reconnaissance geophysical studies of the geothermal systems in southern Raft River valley, Idaho. *Geophysics*, **43**(7), (1978), 1470-1484.

McLeod, I.H., Cumming, I.G., Seymour, M.S.: Envisat ASAR data reduction: Impact on SAR interferometry. *IEEE Trans. Geosci. Remote Sens*, **36** (2), (1998), 589–602.

Maris, V., Wannamaker, P.E., Moore, J.: 3-D Inversion of MT Data From the Raft River Geothermal Field — Preliminary Results. *GRC Trans*. **36**, (2012), 939–942.

Massonnet, D., Holzer, T., Vadon, H.: Land subsidence caused by the East Mesa geothermal field, California, observed using SAR interferometry, Geophys. Res. Lets., **24** (8), (1997), 901-904.

Metternicht, G., Hurni, L., Gogu, R.: Remote sensing of landslides: An analysis of the potential contribution to geo-spatial systems for hazard assessment in mountainous environments. Remote Sensing of Environment, **98**(2-3), (2005), 284-303.

Millar, G.M.: Raft River Geothermal Area Overview. *Geotherm. Resour. Counc. Trans*. **3**, (1979), 461–464.

Mogi, K.: Relation between the eruptions of various volcanoes and deformations of the ground surfaces around them. *Bulletin of Earthquake Research Institute* **36**, (1958), 99-134.

Newman, G.A., Gasperikova, E., Hoversten, G.M., Wannamaker, P.E.: Three-dimensional magnetotelluric characterization of the Coso geothermal field. *Geothermics* **37**, (2008), 369–399. DOI:10.1016/j.geothermics.2008.02.006

Newman, G.A., Petrov, P. V.: 3D VSP Experiment Design Study of the Raft River Geothermal Field, *Proceedings*, the 41st Workshop on Geothermal Reservoir Engineering, Stanford, CA, (2016), SGP–TR–209.

Okada, Y.: Surface deformation due to shear and tensile faults in a half-space. *Int. J. Rock Mech. Min. Sci. Geomech. Abstr.* **75**, (1985) 1135–1154. DOI:10.1016/0148-9062(86)90674-1

Oppliger, G., Coolbaugh, M., Shevenell, L., Taranik, J.: Elucidating deep reservoir geometry and lateral outflow through 3-D elastostatic modeling of satellite radar (InSAR) observed surface deformations: An Example From the Bradys Geothermal Field. *GRC Trans*. **29**, (2005) 419–424.

Prati, C., Ferretti, A., Perissin, D.: Recent advances on surface ground deformation measurement by means of repeated space-borne SAR observations. *Journal of Geodynamics*, **49**(3-4), (2010), 161-170.

Queen, J.H., Daley, T.M., Majer, E.L., Nihei, K.T., Siler, D.L., Faulds, J.E.: Surface Reflection Seismic and Vertical Seismic Profile at Brady ' s Hot Springs , NV , USA, *Proceedings*, the 41st Workshop on Geothermal Reservoir Engineering, Stanford, CA, (2016), SGP–TR–209.

Sarychikina, O., Glowacka, E., Mellors, R., Vidal, F. S.: Land subsidence in the Cerro Prieto Geothermal Field, Baja California, Mexico, from 1994 to 2005: An integrated analysis of DInSAR, leveling and geological data, *J. Volcanol. Geotherm. Res*., **204**, (2011), 76–90.

Settgast, R. R., Fu, P., Walsh, S. D. C., White, J. A., Annavarapu, C., Ryerson, F.J.: A fully coupled method for massively parallel simulation of hydraulically driven fractures in 3-dimensions. *Int. J. Numer. Anal. Meth. Geomech*., (2017), DOI:10.1002/nag.2557.

Spencer, S.G.: Injection at Raft River - An enviromental concern? *Geotherm. Resour. Counc. Trans.* **3**, (1979), 675–678.

Vasco, D.W., Wicks, C., Karasaki, K., Marques, O.: Geodetic imaging: Reservoir monitoring using satellite interferometry. *Geophys. J. Int.* **149**, (2002), 555–571. DOI:10.1046/j.1365-246X.2002.01569.x

Williams, P.L., Covington, H.R., Pierce, K.L.: Cenozoic stratigraphy and tectonic evolution of Raft River Basin, Idaho. *Idaho Bur. Mines Geol. Bull.* **26**, (1982), 491–504.